Global reconstruction reduces the uncertainty of oceanic nitrous oxide emissions and reveals a vigorous seasonal cycle

Simon Yang[a], Bonnie X. Chang[b,c,1], Mark J. Warner[d,1], Thomas S. Weber[e,1], Annie M. Bourbonnais[f], Alyson E. Santoro[g], Annette Kock[h], Rolf E. Sonnerup[b,c], John L. Bullister[c,2], Samuel T. Wilson[i], and Daniele Bianchi[a,3]

[a]Department of Atmospheric and Oceanic Sciences, University of California Los Angeles, CA 90095; [b]Joint Institute for the Study of the Atmosphere and Ocean, University of Washington, Seattle, WA 98195; [c]Pacific Marine Environmental Laboratory, National Oceanic and Atmospheric Administration, Seattle, WA 98115; [d]School of Oceanography, University of Washington, Seattle, WA 98195; [e]Department of Earth and Environmental Sciences, University of Rochester, Rochester, NY 14627; [f]School of the Earth, Ocean and Environment, University of South Carolina, Columbia, SC 29208; [g]Department of Ecology, Evolution, and Marine Biology, University of California, Santa Barbara, CA 93106; [h]Chemical Oceanography Research Unit, GEOMAR Helmholtz Centre for Ocean Research Kiel, 24148 Kiel, Germany; and [i]Center for Microbial Oceanography: Research and Education (C-MORE), University of Hawaii, Honolulu, HI 96822

Edited by François M. M. Morel, Princeton University, Princeton, NJ, and approved April 1, 2020 (received for review December 14, 2019)

Assessment of the global budget of the greenhouse gas nitrous oxide (N_2O) is limited by poor knowledge of the oceanic N_2O flux to the atmosphere, of which the magnitude, spatial distribution, and temporal variability remain highly uncertain. Here, we reconstruct climatological N_2O emissions from the ocean by training a supervised learning algorithm with over 158,000 N_2O measurements from the surface ocean—the largest synthesis to date. The reconstruction captures observed latitudinal gradients and coastal hot spots of N_2O flux and reveals a vigorous global seasonal cycle. We estimate an annual mean N_2O flux of 4.2 $\pm$ 1.0 Tg N·y^{-1}, 64% of which occurs in the tropics, and 20% in coastal upwelling systems that occupy less than 3% of the ocean area. This N_2O flux ranges from a low of 3.3 $\pm$ 1.3 Tg N·y^{-1} in the boreal spring to a high of 5.5 $\pm$ 2.0 Tg N·y^{-1} in the boreal summer. Much of the seasonal variations in global N_2O emissions can be traced to seasonal upwelling in the tropical ocean and winter mixing in the Southern Ocean. The dominant contribution to seasonality by productive, low-oxygen tropical upwelling systems (>75%) suggests a sensitivity of the global N_2O flux to El Niño–Southern Oscillation and anthropogenic stratification of the low latitude ocean. This ocean flux estimate is consistent with the range adopted by the Intergovernmental Panel on Climate Change, but reduces its uncertainty by more than fivefold, enabling more precise determination of other terms in the atmospheric N_2O budget.

nitrous oxide | air–sea gas exchange | seasonal variability | nitrogen cycle | greenhouse gases

N_2O is a greenhouse gas 300 times more potent than CO_2 and the third strongest contributor to radiative forcing from anthropogenic emissions (1). It is also a primary cause of stratospheric ozone depletion (2). Recent syntheses indicate that the oceans account for a third of all natural atmospheric N_2O sources (ref. 3 and *SI Appendix*, Table S1), while the remaining two-thirds are mostly sourced on land (ref. 3 and *SI Appendix*, Table S1). This partitioning has a substantial uncertainty, due to poorly constrained N_2O emissions from both the land and the ocean. Uncertainty in the global oceanic N_2O flux is particularly large, with values reported in the latest Intergovernmental Panel on Climate Change Report (IPCC Fifth Assessment Report [AR5]) ranging from 1.8 to 9.45 Tg N·y^{-1}, a fivefold variation (3). While this large uncertainty reflects the historical scarcity of N_2O measurements and the limitations of earlier estimates, it does not represent the recent progress and community consensus—thus calling for a revised synthesis.

N_2O is produced in the ocean interior by nitrification and denitrification, two processes linked to the remineralization of organic matter. This production is enhanced at low oxygen concentrations and is compensated by N_2O consumption in anoxic waters and emission to the atmosphere when N_2O-laden waters emerge at the surface. Current approaches to estimate the N_2O air–sea flux couple spatial maps of N_2O disequilibrium (ΔpN_2O, the N_2O partial pressure difference across the ocean–atmosphere interface) to wind-dependent models of gas exchange (4–8). In turn, estimates of ΔpN_2O rely on either observational syntheses or numerical models. In observation-based approaches, ΔpN_2O data, calculated from oceanic N_2O concentrations or partial pressures, are extrapolated to the global ocean (4, 5). Model-based approaches calculate ΔpN_2O from coupled ocean circulation–biogeochemical models. Both methods have inherent limitations. Until recently, data coverage was sparse over much of the ocean, in particular, coastal upwelling systems, which host important N_2O air–sea fluxes (5,

Significance

N_2O is a potent greenhouse gas whose oceanic emissions are still poorly constrained. Here, we reconstruct oceanic N_2O emissions from the largest observational synthesis to date, substantially reducing the uncertainty compared to previous estimates and enabling a tightening of the global budget of this gas. We also reveal a vigorous global seasonal cycle, dominated by productive, low-oxygen tropical regions, which suggests sensitivity of the N_2O cycle to natural climate variability and anthropogenic climate change.

Author contributions: S.Y., T.S.W., and D.B. designed research; S.Y. and D.B. performed research; S.Y., B.X.C., M.J.W., A.M.B., A.E.S., A.K., R.E.S., J.L.B., and S.T.W. analyzed data; S.Y. and D.B. wrote the paper; M.J.W., A.M.B., A.E.S., A.K., R.E.S., and J.L.B. collected N_2O measurements; M.J.W. and J.L.B. provided N_2O measurements; A.M.B., A.E.S., A.K., and R.E.S. provided N_2O observations; M.J.W., T.S.W., A.M.B., A.E.S., A.K., R.E.S., J.L.B., and S.T.W. provided inputs for the paper; and S.T.W. organized the Oceanic Methane & Nitrous Oxide Workshop in October 2018, which provided impetus for this work.

The authors declare no competing interest.

This article is a PNAS Direct Submission.

Data deposition: The compilation of N_2O measurements, the reconstructed global Δp_{N_2O} climatology, and N_2O air–sea flux are available for download on the Biological & Chemical Oceanography Data Management Office (BCO-DMO) portal (https://www.bco-dmo.org/dataset/810032 (DOI: 10.26008/1912/bco-dmo.810032.1). The code used to produce these datasets can be found on a public GitHub repository at https://github.com/yangsi7/mapping-ocean-n2o (DOI: 10.5281/zenodo.3757194).

[1]B.X.C., M.J.W., and T.S.W. contributed equally to this work.

[2]Deceased June 13, 2018.

[3]To whom correspondence may be addressed. Email: dbianchi@atmos.ucla.edu.

This article contains supporting information online at https://www.pnas.org/lookup/suppl/doi:10.1073/pnas.1921914117/-/DCSupplemental.

First published May 18, 2020.

9, 10), and much of the polar ocean. In addition, the scarcity of repeated measurements hindered extrapolation of sparse N_2O observations to seasonal timescales. The models in refs. 6–8, which have the advantage of resolving seasonal dynamics, rely on simple representations of the N_2O cycle that poorly represent its sources and sinks in the ocean and are usually too coarse to capture the intense N_2O supersaturation observed in coastal waters (9, 10).

Time series of N_2O measurements have revealed that N_2O air–sea fluxes can have a strong seasonal cycle (11), albeit with substantial regional variability. For example, an extensive survey in the Arabian Sea showed a strong monsoonal modulation of N_2O outgassing (12, 13). Similarly, seasonal variations in atmospheric N_2O in the Southern Ocean can only be explained by seasonality in the underlying ocean circulation (14, 15). This seasonality provides important insights into the drivers of N_2O emissions, but, to date, the global seasonal cycle of oceanic N_2O emissions has only been crudely reconstructed and remains uncertain (4).

In this study, we train a supervised learning algorithm with a large compilation of N_2O measurements to reconstruct the global distribution of N_2O fluxes from well-sampled environmental variables. This reconstruction reveals a vigorous seasonal cycle and captures recently observed hot spots of coastal N_2O emission (9, 10), yielding an understanding of the factors controlling regional N_2O fluxes.

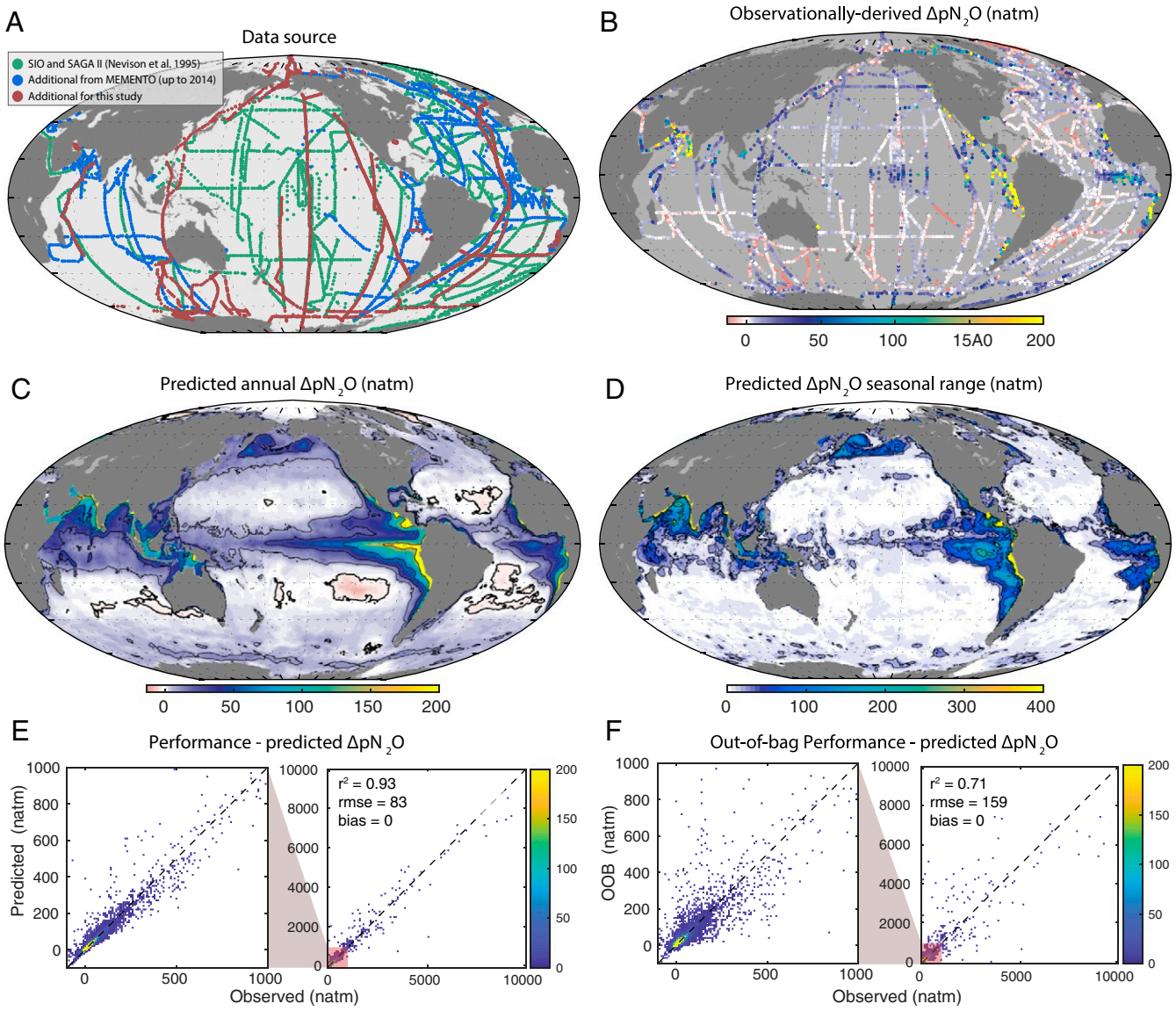

Fig. 1. Observed and reconstructed surface-ocean N_2O supersaturation. (*A*) Location and source of the data. Green dots shows the data used in earlier N_2O flux estimates (4); blue dots show the additional data in the MEMENTO database (16); and red dots are additional data compiled for this study (Dataset S1). (*B*) Observed N_2O supersaturation averaged on a 0.25° grid and expressed as ΔpN_2O (natm). (*C*) Reconstructed annual N_2O supersaturation. (*D*) Reconstructed seasonality of N_2O supersaturation (natm), calculated as the seasonal range over the 12-mo period. (*E*) Performance of the random forest reconstruction shown as two joint distribution plots of predicted vs. observed ΔpN_2O (colors indicate the number of grid points; note the different axis ranges). (*F*) Same as *E*, but using out-of-bag (OOB) predictions, i.e., predictions vs. observations withheld from training (*SI Appendix*, section S1B). Annotations in *E* and *F* show the square of the correlation coefficient (r^2), the rmse and the global bias. Refer to *SI Appendix*, Fig. S1 for the monthly distribution of the data; *SI Appendix*, Figs. S2–S9 for model performance and uncertainty as well as regional zooms; *SI Appendix*, Figs. S10–S12 for seasonal maps and time series of ΔpN_2O, including stereographic projections for polar regions; and Dataset S1 for a comprehensive list of the cruises included in the compilation.

Method Overview

The foundation of our work is a compilation of over 158,000 observations of N_2O mixing ratio, partial pressure, and concentration in the surface ocean (Dataset S1). This compilation, which builds extensively on the Marine Methane and NiTrous Oxide (MEMENTO) database (17), contains close to two times more surface measurements than previous syntheses (5), covering critical, previously undersampled regions (Fig. 1*A*). We estimate the N_2O disequilibrium at the location of each measurement following:

$$\Delta X_{N_2O} = X_{ocean}^{N_2O} - X_{atm}^{N_2O}. \quad [1]$$

Here, $X_{ocean}^{N_2O}$ are ocean-side N_2O measurements converted to mixing ratios, and $X_{atm}^{N_2O}$ is the atmospheric N_2O mixing ratio estimated by interpolating the National Oceanic and Atmospheric Administration (NOAA) atmospheric N_2O flask dataset (18) at the latitude and time of the oceanic measurements (refer to *SI Appendix*, section S1 for detailed methods).

To convert sparse observations to a global climatology, we trained 100 ensembles of regressions trees (random forests) to predict ΔX_{N_2O} based on its relationship to well-sampled physical and biogeochemical predictors. Similar methods have been applied to map the distribution of chemical species in the ocean (19), including the dissolved gas methane (20). The predictors were based on hydrographic variables, nutrients, oxygen, chlorophyll concentrations, net primary production, and seafloor depth and are listed in *SI Appendix*, Table S2. Finally, we express the supersaturation as $\Delta pN_2O = \Delta X_{N_2O} \cdot P$, where P is the local atmospheric pressure, and calculate the N_2O air–sea flux as:

$$\Phi = (1 - f_{ice}) \cdot S \cdot k \cdot \Delta pN_2O, \quad [2]$$

where Φ is the N_2O flux, f_{ice} is the fractional sea ice cover, S is the N_2O solubility, and k is the piston velocity (refer to *SI Appendix*, section S2 for detailed methods). We estimated piston velocities using two wind-speed–dependent parameterizations: an updated version of a commonly used quadratic formulation (21, 22) and a recent formulation that explicitly accounts for the effect of bubble-mediated fluxes (23). We applied each parameterization to two high-resolution wind products (24, 25) that are available at 0.25°, 6-hourly resolution for the period from 1988 to 2017, yielding four permutations of the piston velocity (*SI Appendix*, section S2). In total, we obtained an ensemble of 400 global N_2O air–sea flux estimates, from which we calculated a mean and uncertainty range.

Results and Discussion

ΔpN_2O.

Annual mean distribution. The ensemble mean prediction reproduces ΔpN_2O extremely faithfully (r^2 = 0.92; *SI Appendix*, Fig. S2), while maintaining high generalization; observations that were withheld from the training step of the algorithm were predicted with an r^2 of 0.70, an rms error (rmse) of ∼ 159 natm (32 natm excluding waters from the Peruvian upwelling) and a negligible global bias (∼0.01 natm; *SI Appendix*, Figs. S2–S5 and S7–S9). Consistent with previous work (4, 8, 26), we found that large swaths of the surface ocean are supersaturated with N_2O, including productive upwelling regions, the subpolar Pacific, and the Southern Ocean. Slight supersaturation and occasional undersaturation are predicted in the subtropical gyres (Fig. 1*C*). Undersaturation also characterizes the open Arctic Ocean, while its shelves, in particular, the East Siberian Shelf, are supersaturated. An aspect of our reconstruction is the ability to capture narrow bands of strong supersaturation observed in Eastern Boundary Upwelling Systems (Fig. 1 *A* and *C*), particularly along the western coast of India (27), Namibia (10), and Peru (9). There, some of the highest ΔpN_2O ever observed, in excess of 8,000 natm, were successfully reproduced (*SI Appendix*, Figs. S2, S3, and S9).

We estimated the relative importance of each of the predictors by performing a recursive feature elimination for all potential predictor combinations (*SI Appendix*, section S1C). We found that chlorophyll, subsurface oxygen, and subsurface apparent oxygen utilization (AOU) were the features with highest predictive power for our ΔpN_2O dataset. A model trained with these three predictors alone can explain over 60% of the variance in observed ΔpN_2O (*SI Appendix*, Fig. S6). The importance of these predictors is consistent with N_2O production from nitrification and denitrification, which are enhanced in high-productivity, low-O_2 waters (28).

ΔpN_2O seasonality and drivers. The annual mean reconstruction of ΔpN_2O hides a dynamic seasonal cycle (Fig. 1*D*), with a range generally proportional to the mean saturation of the waters (Fig. 1*C*).

Accordingly, the largest seasonal ΔpN_2O excursions are found over the coastal waters of Peru, the Arabian Sea, and the Costa Rica Dome, where ΔpN_2O can change by over 500 natm over the course of the year. Significant ΔpN_2O excursions (in excess of 200 natm) are also found in the central Arabian Sea, the Bay of Bengal, the subpolar Pacific, and the Eastern Tropical Pacific and Atlantic.

We investigated the drivers of this seasonality by analyzing the patterns of temporal correlation between ΔpN_2O and four of its predictors: chlorophyll, subsurface AOU, mixed-layer depth, and sea-surface temperature (SST) (Fig. 2 and *SI Appendix*, Fig. S14). The signs of the four correlation coefficients (positive or negative), in combination, allowed us to identify four empirical regimes of ΔpN_2O seasonality (Fig. 2). The first regime

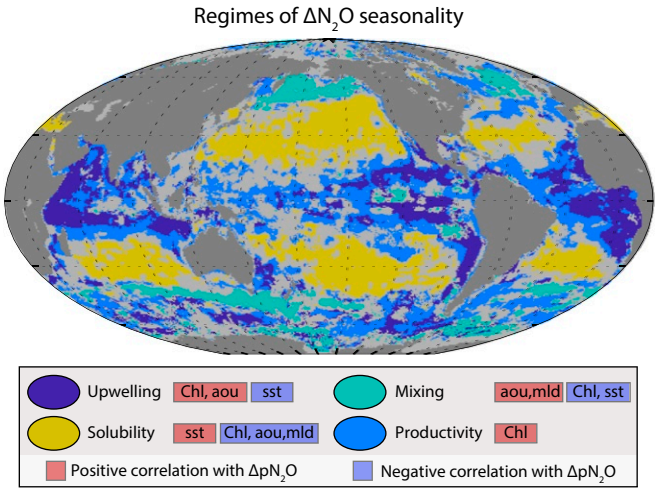

Fig. 2. Empirical drivers of ΔpN_2O seasonality. Potential drivers are labeled based on temporal correlations between ΔpN_2O and four environmental predictors: log(Chlorophyll) (Chl), SST, AOU, and mixed-layer depth (mld). Positive correlations are indicated by a red box and negative correlations by a blue box. Four primary regimes are identified: *1*) Upwelling (navy blue), where seasonal changes in ΔpN_2O are positively correlated with Chl and AOU, but negatively correlated with SST; *2*) mixed-layer depth (turquoise), where ΔpN_2O is positively correlated with mld and AOU, but negatively correlated with Chl and SST; *3*) solubility (yellow), where ΔpN_2O is positively correlated with SST only; and *4*) productivity (blue), which encompasses regions with positive correlations between ΔpN_2O and Chl that do not fit in the three previous regimes. Regime (1) is constrained to a minimum annual chlorophyll concentration of 0.1 mg m^{-3} to exclude parts of the subtropical gyres. See *SI Appendix*, section S1B for detailed methods and *SI Appendix*, Fig. S14 for maps of the individual correlations.

spans the majority of the tropical and northern Indian Ocean, the eastern tropical Pacific and Atlantic Oceans, and parts of the Southern Ocean (navy blue regions in Fig. 2). In these regions, ΔpN_2O changes are positively correlated with chlorophyll and subsurface AOU, but negatively correlated with SST, suggesting an important role for upwelling, which brings cold, nutrient-rich, high-AOU waters close to the surface (Fig. 2 and *SI Appendix*, Fig. S14). Consistent with this interpretation, ΔpN_2O values in the Indian Ocean, particularly over the coastal Arabian Sea and Bay of Bengal, peak during the upwelling-favorable Southwest Monsoon in the late boreal summer (*SI Appendix*, Figs. S11–S13). The second regime mostly covers deep mixed-layer systems, including the Southern Ocean Polar Front, and the subpolar Atlantic and Pacific (turquoise regions in Fig. 2). In these regions, ΔpN_2O peaks during winter, when chlorophyll and temperature are low, and deep mixed layers expose high-AOU, N_2O-rich waters to the atmosphere (Fig. 2 and *SI Appendix*, Fig. S13). The third regime is found over the ocean's subtropical gyres, where the seasonality of ΔpN_2O follows that of SST, but is in opposite phase with all other predictors (yellow regions in Fig. 2). The positive correlation with SST (average slope of 1 natm/0.13 °C) suggests that changes in N_2O solubility caused by seasonal warming or cooling drive seasonal changes in ΔpN_2O (Fig. 2 and *SI Appendix*, Fig. S13), a result

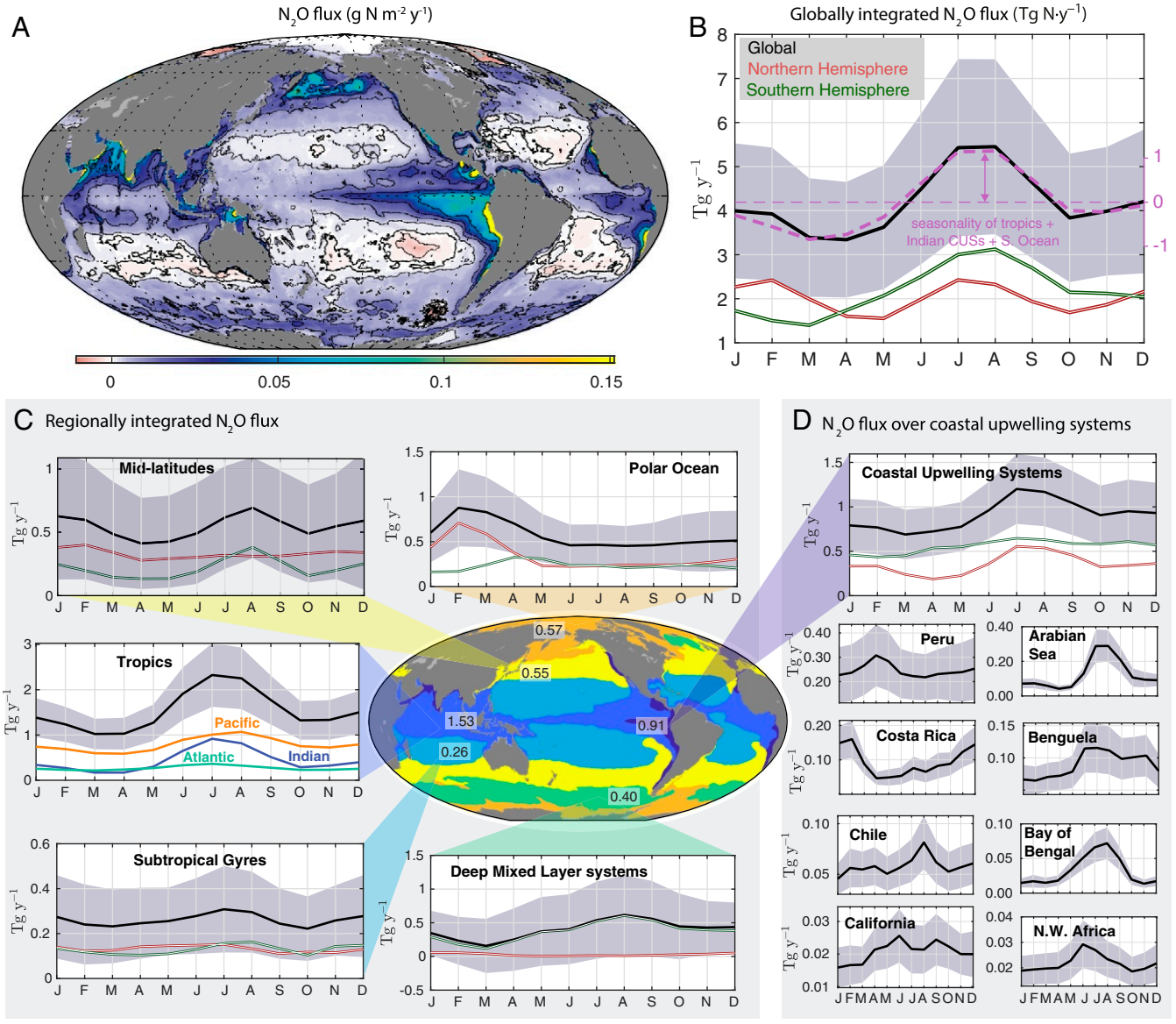

Fig. 3. Reconstructed N_2O air–sea flux. (*A*) Annual mean N_2O flux ($g \cdot m^{-2} \cdot y^{-1}$; see also *SI Appendix*, Fig. S15). (*B*) Climatology of the N_2O flux ($Tg\ N \cdot y^{-1}$) for the global ocean (black), the Northern Hemisphere (red), and the Southern Hemisphere (green). The purple dashed line shows the combined seasonal anomalies of the Tropical ocean biome [see *C* for a definition of biomes], the upwelling systems of the Arabian Sea and the Bay of Bengal (CUSs, coastal upwelling systems), and the Southern (S.) Ocean deep mixed-layer biome (vertical axis on the right, with 0 centered at value 4.2 $Tg\ N \cdot y^{-1}$ on the left axis, i.e., the global mean flux). (*C* and *D*) Climatological N_2O fluxes ($Tg\ N \cdot y^{-1}$) for six major biomes (Tropics, Coastal Upwelling Systems, Mid-Latitudes, Subtropical Gyres, Deep Mixed-Layer Systems, and Polar Ocean; refer to *SI Appendix*, section S4A for detailed methods). Red and green lines show integrals over the Northern and Southern Hemispheres, respectively; orange, blue, and turquoise lines show the contribution of the Indian, Pacific, and Atlantic, respectively, to the Tropical biome. Numbers on the map show annual mean N_2O fluxes integrated over each biome. In *D*, climatologies for individual coastal upwelling systems are also shown (refer to *SI Appendix*, section S4A and Fig. S13). N.W., northwest. In *B*–*D*, envelopes around the black lines show the uncertainty.

consistent with previous findings (29). The majority of regions that are not assigned to the three previous regimes exhibited a positive correlation between seasonal cycles of pN_2O and chlorophyll, suggesting that local N_2O production during organic-matter cycling may control the surface disequilibrium, although this cannot be proven in the current analysis. We aggregated these waters into a fourth, productivity-driven regime (blue regions in Fig. 2), which often acts as a buffer between the upwelling, solubility, and mixed-layer regimes. Some upwelling systems also fall under the productivity-driven regime, including along Peru and California, where the seasonal cycle of chlorophyll is at least partially decoupled from that of SST and mixed-layer depth (30).

N_2O Flux.

Annual mean distribution. The reconstructed N_2O air–sea flux (Fig. 3) shows that most of the ocean is a source of N_2O to the atmosphere, in particular, in the tropics, coastal upwelling systems, and subpolar regions. These patterns closely mirror those of ΔpN_2O, but with a relative amplification in regions of high winds, such as the mid to high latitudes. We estimated a global annual mean air–sea flux of N_2O of 4.2 $\pm$ 1.0 Tg $N{\cdot}y^{-1}$. This figure is consistent with earlier data-based estimates of about 4 (1.2 to 6.8) Tg $N{\cdot}y^{-1}$ (4, 5) and the IPCC range of 1.8 to 9.45 Tg $N{\cdot}y^{-1}$ (3), but with a much reduced uncertainty. We trace most of the uncertainty in our estimate to the piston velocity formulation, the winds, and ΔpN_2O, in order of importance (*SI Appendix*, section S2D and Fig. S18).

Despite the similarity of our global estimate to previous studies (4, 5), we reconstructed a dramatically different spatial distribution. Low latitudes (30°S to 30°N) contribute 64% of the global flux (2.7 Tg $N{\cdot}y^{-1}$), ~60% higher than previous estimates (4, 5). We further revealed the outsize role of coastal upwelling systems, where intense outgassing drives over 20% of the global N_2O flux, despite covering only 3% of the world's oceans (Fig. 3*D*). Waters off the coast of Peru alone contribute nearly 0.25 Tg $N{\cdot}y^{-1}$, a magnitude consistent with the lower end of a recent regional estimate (9). They are followed by waters in the coastal Arabian Sea and off Costa Rica, which emit 0.13 and 0.09 Tg $N{\cdot}y^{-1}$, respectively. Reconstructions for the coastal Arabian Sea, Benguela, California, and Mauritanian upwelling systems fall within the range of previous observational estimates (refs. 10 and 31–33 and *SI Appendix*, Table S3).

The remaining 36% of the global N_2O flux is distributed approximately equally between hemispheres, yielding only a 19% contribution from the Southern Ocean (south of 30°S), about half of previous estimates (4, 5). We suggest that sampling biases are behind previous overestimates of N_2O fluxes in this region. The Southern Ocean is heavily sampled in the summer and late winter, when N_2O outgassing is the largest, and undersampled in the fall, when N_2O outgassing rapidly drops to negligible values (ref. 5 and Fig. 3*C*). This result highlights the limitations of previous approaches based on direct extrapolation of sparse measurements, compared to the statistical models that we apply here.

N_2O flux seasonality and drivers. Our reconstruction revealed that the global air–sea flux of N_2O undergoes a vigorous and previously unappreciated seasonal cycle, increasing from a minimum of 3.3 $\pm$ 1.3 Tg $N{\cdot}y^{-1}$ in the boreal spring to a maximum of 5.5 $\pm$ 2.0 Tg $N{\cdot}y^{-1}$ in the boreal summer, with a secondary maximum in December (4.2 $\pm$ 1.6 Tg $N{\cdot}y^{-1}$). This global cycle emerges from nearly synchronous seasonal changes in the Indian Ocean, the tropical Pacific, and the Southern Ocean. The Indian Ocean alone contributes ~1.1 Tg $N{\cdot}y^{-1}$, or about half of the increase in the global flux from boreal spring to summer, i.e., the Southwest Monsoon season. A large portion of this increase originates in the Arabian Sea (~0.44 Tg $N{\cdot}y^{-1}$), particularly near the coast (~0.23 Tg $N{\cdot}y^{-1}$), which accounts alone for ~14% of the global flux increase from March to August. The tropical Pacific and the Southern Ocean contribute another ~23% and ~17%, respectively, or an increase by ~0.5 and ~0.4 Tg $N{\cdot}y^{-1}$ from the late austral summer to the austral winter, when stronger trade winds over the Pacific and deeper mixed layers in the Southern Ocean expose older, N_2O-rich waters to the atmosphere (Fig. 3*C*). The remaining contribution mostly stems from the northern midlatitudes, where increased productivity from late spring to summer fuels excess N_2O production and release to the atmosphere (Fig. 3*C*). The secondary global peak in boreal winter emerges from multiple regional contributions, in particular, in the Subpolar Pacific, northern midlatitudes, and Southern Ocean. These wintertime enhancements reflect different regional drivers: deeper mixing in the North Pacific, more vigorous winds over midlatitudes, and increased summertime primary production in the Southern Ocean (Fig. 2).

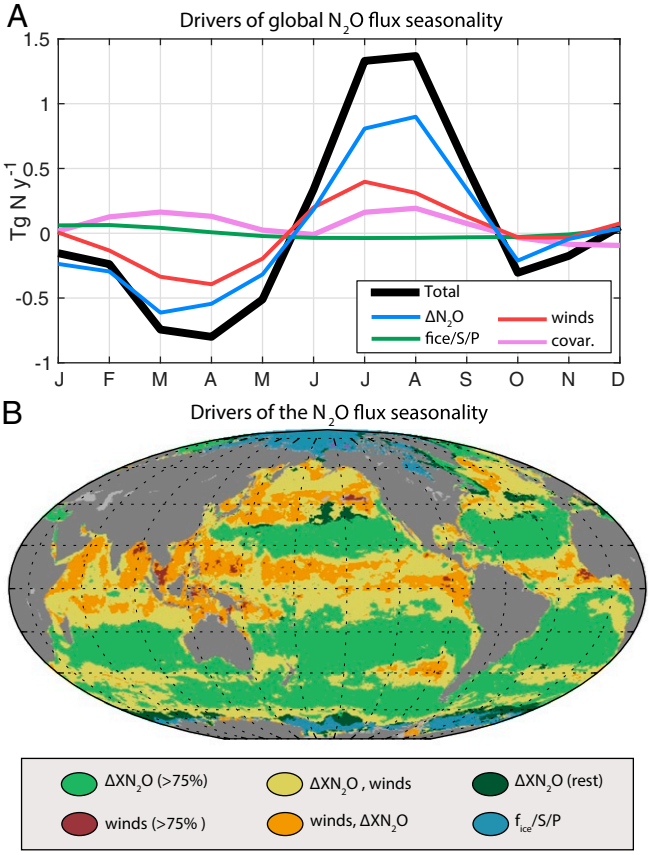

Fig. 4. Drivers of the N_2O flux seasonality. (*A*) Total N_2O flux deviation from the annual mean (black line) and its components (*SI Appendix*, Eq. **S17**) driven by changes in disequilibrium (ΔX_{N_2O}; blue line); wind speed (red line); sea-ice cover, N_2O solubility, and sea-level pressure (f_{ice}, Sa, and P; green line); and covariations (covar.) of all previous terms (pink line). See *SI Appendix*, section S3 and Eqs. **S19** and **S20** for a description of this decomposition. (*B*) Contribution of different drivers to N_2O flux seasonality. In dark green, regions where changes in ΔX_{N_2O} contribute over 75%; in red, regions where changes in winds contribute over 75%; in yellow, regions where ΔX_{N_2O} and winds are, respectively, the primary and secondary driver; in orange, regions where winds and ΔX_{N_2O} are, respectively, the primary and secondary driver; in dark green, regions where ΔX_{N_2O} is the primary driver, followed by a driver other than wind; and in blue, regions where f_{ice}, Sa, and P are the primary drivers. Contributions from individual drivers are shown in *SI Appendix*, Fig. S17.

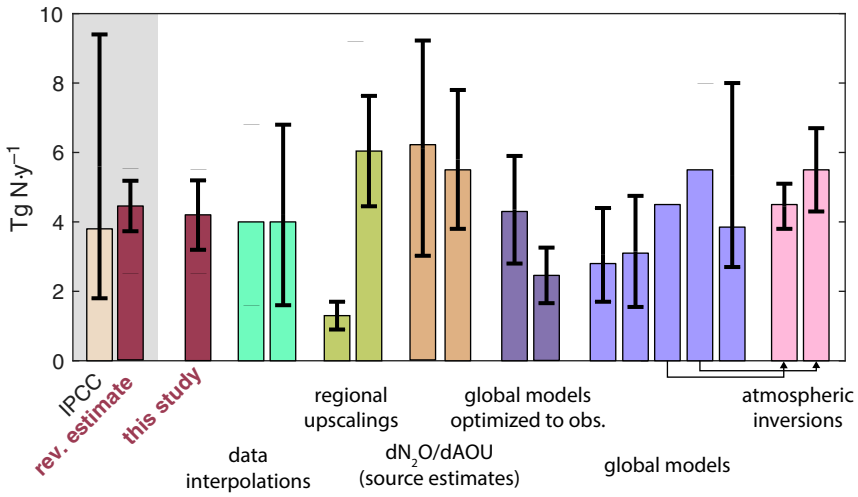

Fig. 5. Estimates of global oceanic N_2O emissions (Tg N·y^{-1}), grouped by method. Light green, data interpolations (4, 5); dark green, extrapolations of regional observations (39, 40); light brown, interior estimates based on the relationships between dissolved N_2O and AOU (28, 34); light purple, global ocean models (7, 37, 38, 41, 42); dark purple, global ocean models optimized by N_2O observations (6, 7, 8); pink, atmospheric inversions (35, 36). Black arrows connect global ocean models to atmospheric inversions that use them as priors. Our study (a databased reconstruction) is shown in brown. The revised (rev.) estimate next to the IPCC AR5 value (3) is based on an average of all categories, as discussed in the main text and *SI Appendix*.

We further investigated the seasonal modulation of N_2O fluxes by decomposing flux variations into four components (*SI Appendix*, section S3 and Eqs. **S16** and **S17**), respectively, driven by seasonal variations in *1*) sea-ice cover, solubility, and sea-level pressure; *2*) wind speed; *3*) disequilibrium (ΔX_{N_2O}); and *4*) covariations between the previous terms. We find that, on average, over two-thirds of the global flux seasonality are driven by changes in ΔX_{N_2O}, with the remaining one-third driven by changes in wind speed (Fig. 4*A*). Solubility, sea-ice cover, and atmospheric pressure contribute minimally to seasonality, and covariations, while dampening seasonality in the boreal spring, enhance it in the boreal summer, resulting in a small net effect (Fig. 4*A*). Changes in ΔX_{N_2O} are the primary driver of seasonality over most of the ocean, with some notable exceptions (Fig. 4*B*). First, in the tropics, sub-Arctic regions, and some portions of the Southern Ocean, winds are either the primary driver or a close secondary driver (Fig. 4*B*). Second, in the seasonal sea-ice zones around Antarctica and the Arctic coastline, N_2O flux variations are mostly driven by changes in sea-ice cover (Fig. 4*B*).

Converging Estimates of Oceanic N_2O Flux Emissions. Our global N_2O emission of 4.2 Tg N·y^{-1} is comparable to previous reconstructions based on surface-data interpolations (4, 5), although with a significantly more extensive set of observations and reduced uncertainty. It also overlaps with estimates based on N_2O production in the ocean interior (28, 34), which use independent subsurface N_2O observations, but cannot be constrained as tightly. Finally, it is highly consistent with atmospheric inversions (35, 36), which update prior estimates based on numerical ocean models (37, 38) to leverage the strong, independent constraint of atmospheric N_2O concentrations. Combining results from all these different methods (*SI Appendix*) revises the global oceanic N_2O flux to 4.4 ± 0.7 Tg N·y^{-1}—a value indistinguishable from our reconstruction and a fivefold reduction in uncertainty compared to the range (1.8 to 9.4 Tg N·y^{-1}) adopted by the IPCC AR5 (Fig. 5).

Implications and Conclusions

Our synthesis of N_2O measurements—the largest to date—reveals a vigorous seasonal cycle of oceanic N_2O emissions, with an excursion of 2.1 Tg N·y^{-1}, half of the global annual mean. Much of these emissions and their seasonal variability can be traced to tropical regions and upwelling systems, where productive waters overlay shallow oxygen minima (43). The sensitivity of tropical N_2O emissions to seasonal variations suggests a similar sensitivity to the El Niño-Southern Oscillation and the Pacific Decadal Oscillation, which modulate productivity and the depth of tropical oxygen minima on interannual to multidecadal timescales (43, 44). Reconstructing the sensitivity of oceanic N_2O emissions to these modes of natural climate variability would, in turn, shed light on their response to anthropogenic climate change, which is projected to increase thermal stratification and reduce productivity in the tropics (45). Such reconstructions would likely benefit from long-term measurements, targeting regions with large fluxes and seasonality (Figs. 2 and 3).

The reduced uncertainty of our oceanic N_2O emissions estimate and its ability to capture seasonal variations and coastal hot spots make it ideal for use as a prior in atmospheric inversions of land-based N_2O fluxes (35). This would translate into tighter estimates of other terms in the atmospheric N_2O budget, including better constraints on anthropogenic N_2O emissions.

Materials and Methods

The compilation of N_2O measurements, the reconstructed global Δp_{N_2O} climatology, and N_2O air–sea flux are available for download on the BCO-DMO portal (https://www.bco-dmo.org/dataset/810032). The code used to produce these datasets can be found on a public GitHub repository, https://github.com/yangsi7/MappingDN2OandFlux. Refer to *SI Appendix*, section S1B and Table S2 for detailed methods, including information on published datasets used to train the random forest model and compute the flux.

ACKNOWLEDGMENTS. S.Y. and D.B. were supported by NSF Grants 1635632 and 1847687 and Swiss National Science Foundation Grant P2EZP2_172166. This publication is partially funded by the Joint Institute for the Study of the Atmosphere and Ocean under the NOAA Cooperative Agreement NA15OAR4320063, Contribution 2019-1038 (Pacific Marine Environmental Laboratory Contribution 5047). We thank the administrators and individual contributors of all of the data products used in the manuscript, as listed in *SI Appendix*. We also acknowledge the Ocean Carbon and Biogeochemistry Project Office, supported by NSF Grant 1558412 and NASA Grant NNX17AB17G, for organizing the Oceanic Methane & Nitrous Oxide Workshop in October 2018, which provided impetus for this work. This work used the Extreme Science and Engineering Discovery Environment, which is supported by NSF Grant ACI-1548562.

1. G. Myhre *et al.*, "Anthropogenic and natural radiative forcing in climate change 2013: The physical science basis" in *Working Group I Contribution to the Fifth Assessment Report of the Intergovernmental Panel on Climate Change*, T. F. Stocker *et al.*, Eds. (Cambridge University Press, Cambridge, UK, 2014), pp. 659–740.
2. R. W. Portmann, J. S. Daniel, A. R. Ravishankara, Stratospheric ozone depletion due to nitrous oxide: Influences of other gases. *Philos. Trans. R. Soc. London. Series B, Biol. Sci.* **367**, 1256–1264 (2012).
3. P. Ciais *et al.*, "Carbon and other biogeochemical cycles in climate change 2013—The physical science basis" in *Working Group I Contribution to the Fifth Assessment Report of the Intergovernmental Panel on Climate Change*, T. F. Stocker *et al.*, Eds. (Cambridge University Press, Cambridge, UK, 2014), pp. 465–570.
4. C. D. Nevison, R. F. Weiss, D. J. Erickson III, Global oceanic emissions of nitrous oxide. *J. Geophys. Res. Oceans* **100**, 15809–15820 (1995).
5. C. D. Nevison, T. J. Lueker, R. F. Weiss, Quantifying the nitrous oxide source from coastal upwelling. *Global Biogeochem. Cycles* **18**, GB1018 (2004).
6. G. Battaglia, F. Joos, Marine N_2O emissions from nitrification and denitrification constrained by modern observations and projected in multimillennial global warming simulations. *Global Biogeochem. Cycles* **32**, 92–121 (2018).
7. Q. Ji, E. Buitenhuis, P. Suntharalingam, J. L. Sarmiento, B. B. Ward, Global nitrous oxide production determined by oxygen sensitivity of nitrification and denitrification. *Global Biogeochem. Cycles* **32**, 1790–180 (2018).
8. E. T. Buitenhuis, P. Suntharalingam, C. Le Quéré, Constraints on global oceanic emissions of N_2O from observations and models. *Biogeosciences* **15**, 2161–2175 (2018).
9. D. L. Arevalo-Martinez, A. Kock, C. R. Loscher, R. A. Schmitz, H. W. Bange, Massive nitrous oxide emissions from the tropical South Pacific Ocean. *Nature Geosci* **8**, 530–533 (2015).
10. D. L. Arévalo-Martínez *et al.*, N_2O emissions from the northern Benguela upwelling system. *Geophys. Res. Lett.* **46**, 3317–3326 (2019).
11. L. Farías, V. Besoain, S. García-Loyola, Presence of nitrous oxide hotspots in the coastal upwelling area off central Chile: An analysis of temporal variability based on ten years of a biogeochemical time series. *Environ. Res. Lett.* **10**, 44017 (2015).
12. S. Lal, P. K. Patra, Variabilities in the fluxes and annual emissions of nitrous oxide from the Arabian Sea. *Global Biogeochem. Cycles* **12**, 321–327 (1998).
13. R. C. Upstill-Goddard, J. Barnes, N. J. P. Owens, Nitrous oxide and methane during the 1994 SW monsoon in the Arabian Sea/northwestern Indian Ocean. *J. Geophys. Res. Oceans* **104**, 30067–30084 (1999).
14. X. Jin, N. Gruber, Offsetting the radiative benefit of ocean iron fertilization by enhancing N_2O emissions. *Geophys. Res. Lett.* **30**, 2249 (2003).
15. C. D. Nevison *et al.*, Southern Ocean ventilation inferred from seasonal cycles of atmospheric N_2O and O_2/N_2 at Cape Grim, Tasmania. *Tellus B* **57**, 218–229 (2005).
16. H. W. Bange *et al.*, MEMENTO: A proposal to develop a database of marine nitrous oxide and methane measurements (MEMENTO database accessed via https://memento.geomar.de in March 2019). *Environ. Chem.* **6**, 195–197 (2009).
17. A. Kock, H. W. Bange, Counting the ocean's greenhouse gas emissions. *Eos* **96** (2015).
18. B. D. Hall, G. S. Dutton, J. W. Elkins, The NOAA nitrous oxide standard scale for atmospheric observations. *J. Geophys. Res.: Atmospheres* **112**, D09305 (2007).
19. T. Shserwen *et al.*, A machine-learning-based global sea-surface iodide distribution. *Earth Syst. Sci. Data* **11**, 1239–1262 (2019).
20. T. Weber, N. A. Wiseman, A. Kock, Global ocean methane emissions dominated by shallow coastal waters. *Nat. Commun.* **10**, 4584 (2019).
21. R. Wanninkhof, Relationship between wind speed and gas exchange over the ocean. *J. Geophys. Res. Oceans* **97**, 7373–7382 (1992).
22. R. Wanninkhof, Relationship between wind speed and gas exchange over the ocean revisited. *Limnol Oceanogr. Methods* **12**, 351–362 (2014).
23. J. H. Liang *et al.*, Parameterizing bubble-mediated air-sea gas exchange and its effect on ocean ventilation. *Global Biogeochem. Cycles* **27**, 894–905 (2013).
24. Copernicus Climate Change Service (C3S) (2017): ERA5: Fifth generation of ECMWF atmospheric reanalyses of the global climate. Copernicus Climate Change Service Climate Data Store (CDS). https://cds.climate.copernicus.eu/cdsapp#!/home. Accessed 24 February 2019.
25. Remote Sensing Systems Cross-Calibrated Multi-Platform (CCMP) 6-hourly ocean vector wind analysis product on 0.25 deg grid, Version 2.0. http://www.remss.com/measurements/ccmp/. Accessed 1 May 2019.
26. P. Suntharalingam, J. L. Sarmiento, Factors governing the oceanic nitrous oxide distribution: Simulations with an ocean general circulation model. *Global Biogeochem. Cycles* **14**, 429–454 (2000).
27. H. W. Bange *et al.*, Nitrous oxide emissions from the Arabian Sea: A synthesis. *Atmos. Chem. Phys.* **1**, 61–71 (2001).
28. C. Nevison, J. H. Butler, J. W. Elkins, Global distribution of N_2O and the ΔN_2O-AOU yield in the subsurface ocean. *Global Biogeochem. Cycles* **17**, 1119 (2003).
29. S. T. Wilson, S. Ferrón, D. M. Karl, Interannual variability of methane and nitrous oxide in the North Pacific Subtropical Gyre. *Geophys. Res. Lett.* **44**, 9885–9892 (2017).
30. V. Echevin, O. Aumont, J. Ledesma, G. Flores, The seasonal cycle of surface chlorophyll in the Peruvian upwelling system: A modelling study. *Prog. Oceanogr.* **79**, 167–176 (2008).
31. S. W. A. Naqvi *et al.*, Increased marine production of N_2O due to intensifying anoxia on the Indian continental shelf. *Nature* **408**, 346–349 (2000).
32. T. J. Lueker, Coastal upwelling fluxes of O_2, N_2O, and CO_2 assessed from continuous atmospheric observations at Trinidad, California. *Biogeosciences* **1**, 101–111 (2004).
33. F. Wittke, A. Kock, H. W. Bange, Nitrous oxide emissions from the upwelling area off Mauritania (NW Africa). *Geophys. Res. Lett.* **37**, L12601 (2010).
34. D. Bianchi, J. P. Dunne, J. L. Sarmiento, E. D. Galbraith, Data-based estimates of suboxia, denitrification, and N_2O production in the ocean and their sensitivities to dissolved O_2. *Global Biogeochem. Cycles* **26**, GB2009 (2012).
35. E. Saikawa *et al.*, Global and regional emissions estimates for N_2O. *Atmos. Chem. Phys.* **14**, 4617–4641 (2014).
36. R. L. Thompson *et al.*, Nitrous oxide emissions 1999 to 2009 from a global atmospheric inversion. *Atmos. Chem. Phys.* **14**, 1801–1817 (2014).
37. S. Dutreuil, L. Bopp L., A. Tagliabue, Impact of enhanced vertical mixing on marine biogeochemistry: Lessons for geo-engineering and natural variability. *Biogeosciences* **6**, 901–912 (2009).
38. M. Manizza M., R. F. Keeling R. F., C. D. Nevison C. D., On the processes controlling the seasonal cycles of the air-sea fluxes of O_2 and N_2O: A modelling study. *Tellus Ser. B Chem. Phys. Meteorol.*, 10.3402/tellusb.v64i0.18429 (2012).
39. H. W. Bange, S. Rapsomanikis, M. O. Andreae, Nitrous oxide in coastal waters. *Global Biogeochem. Cycles* **10**, 197–207 (1996).
40. T. S. Rhee, A. J. Kettle, M. O. Andreae, Methane and nitrous oxide emissions from the ocean: A reassessment using basin-wide observations in the Atlantic. *J. Geophys. Res.: Atmospheres* **114**, D12304 (2009).
41. P. Suntharalingam, J. L. Sarmiento, J. R. Toggweiler, Global significance of nitrous-oxide production and transport from oceanic low-oxygen zones: A modeling study. *Global Biogeochem. Cycles* **14**, 1353–1370 (2000).
42. L. M. Zamora, A. Oschlies, Surface nitrification: A major uncertainty in marine N_2O emissions. *Geophys. Res. Lett.* **41**, 4247–4253 (2014).
43. C. Deutsch, H. Brix, T. Ito, H. Frenzel, L. Thompson, Climate-forced variability of ocean hypoxia. *Science (New York, N.Y.)* **333**, 336–339 (2011).
44. S. Yang, N. Gruber, M. C. Long, M. Vogt, ENSO-driven variability of denitrification and suboxia in the Eastern Tropical Pacific Ocean. *Global Biogeochem. Cycles* **31**,1470–1487 (2017).
45. L. Bopp, *et al.*, Multiple stressors of ocean ecosystems in the 21st century: Projections with CMIP5 models. *Biogeosciences* **10**, 6225–6245 (2013).